ACS APPLIED MATERIALS & INTERFACES

www.acsami.org

Research Article

Enhanced Removal of Cu^{2+} and Pb^{2+} Ions from Wastewater via a Hybrid Capacitive Deionization Platform with MnO_2/N-Doped Mesoporous Carbon Nanocomposite Electrodes

Jie Jin, Yang Bao, and Feihu Li*

Cite This: *ACS Appl. Mater. Interfaces* 2025, 17, 13783−13793

Read Online

ACCESS | Metrics & More | Article Recommendations | Supporting Information

ABSTRACT: Integrating MnO_2 with carbon is a reliable strategy to improve capacitive deionization (CDI) performance by leveraging the unique properties of both components (i.e., MnO_2 and carbon). However, the influences of preliminary functionalization of carbon (e.g., nitrogen doping, KOH activation) and pairing of cathodes and anodes on the CDI performance have yet to be systematically explored. Herein, we prepared a group of MnO_2-decorated mesoporous carbon composites with nitrogen as a dopant (i.e., MK-NMCS, K-NMCS, NMCS, and CS), and systematically evaluated the desalination performance of various cathode//anode pairs in a hybrid capacitive deionization (HCDI) for capturing Na^+, Cu^{2+}, and Pb^{2+}, respectively. Of all electrodes, the MK-NMCS//K-NMCS pair demonstrates the optimum desalination performance based on salt adsorption capacity (SAC) and cycling stability, offering a SAC of 25.4 mg g^{-1} and a SAC retention of 102.4% after 50 consecutive charge−discharge cycles at 1.2 V in 500 ppm of NaCl solution. In addition, the MK-NMCS//K-NMCS electrodes also show the maximum ion adsorption capacity (IAC) toward Cu^{2+} and Pb^{2+} ions compared to other cathode//anode pairs, attaining an IAC of 37.0 and 30.0 mg Cu^{2+} per gram electrode materials at 1.2 V in 500 and 200 ppm of Cu^{2+} solutions, respectively (cf. 32.2 mg of Pb^{2+} per gram of electrode materials in 200 ppm of Pb^{2+} solution). Besides, these electrodes exhibit excellent cycling stability when applied in removing each heavy metal ion separately, with IAC retentions of 90.0 and 98.5% after 50 cycles toward Cu^{2+} and Pb^{2+} ions, respectively. Mechanical analysis reveals that both heavy metals are likely to be sequestered via capacitive electrosorption by carbon, intercalation with MnO_2, and surface complexation at the external surface of the $[MnO_6]$ octahedral layers. Our results demonstrated a great potential of the MnO_2-decorated N-doped carbon//prefunctionalized carbon pairs, in particular, the MK-NMCS//K-NMCS electrode pair for capturing heavy metal ions via HCDI platforms. Such prefunctionalization and pairing strategies are very promising for screening high-performance composite electrodes for wastewater remediation.

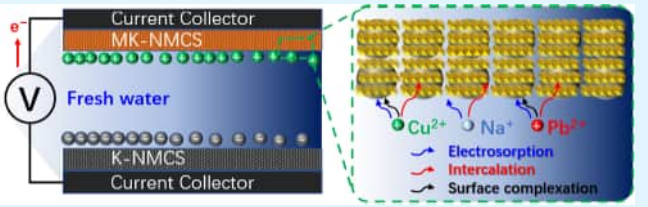

KEYWORDS: *copper, lead, hybrid capacitive deionization (HCDI), birnessite, intercalation*

1. INTRODUCTION

The global water shortage, deteriorated by climate change and water pollution, has become a critical concern impacting many regions worldwide.[1−3] Climate change contributes to this crisis by altering precipitation patterns, resulting in more frequent and severe droughts, and disrupting the natural water cycle.[4] Concurrently, water pollution further exacerbates the scarcity of freshwater.[5] Among the various pollutants, heavy metals pose a significant threat to water bodies. Rivers, for example, which are vital sources of freshwater, are particularly vulnerable.[6] When contaminated by heavy metals, such as copper (Cu^{2+}) and lead (Pb^{2+}), these rivers will inevitably experience severe ecological damage.[6,7] Heavy metals are toxic to macroscopic organisms, leading to their rapid death. This, in turn, impacts microorganisms essential for the river's self-purification processes, ultimately diminishing the river's ability to recover its health over time.[8] The contamination of rivers with heavy metals has profound consequences for both the environment and human health. Copper and lead ions, for example, are notorious for their harmful effects. Copper, when present in high concentrations, can disrupt aquatic ecosystems, causing detrimental effects on fish and plant life, while also posing risks to human health, such as gastrointestinal distress and liver damage.[9] Lead ions are even more dangerous; they can accumulate in the food chain, leading to severe neurological and developmental issues, particularly in children.[10] The persistence of these metals in the environment further complicates this issue, making remediation efforts crucial.

Received: October 29, 2024
Revised: February 17, 2025
Accepted: February 17, 2025
Published: February 21, 2025

https://doi.org/10.1021/acsami.4c18755
ACS Appl. Mater. Interfaces 2025, 17, 13783−13793

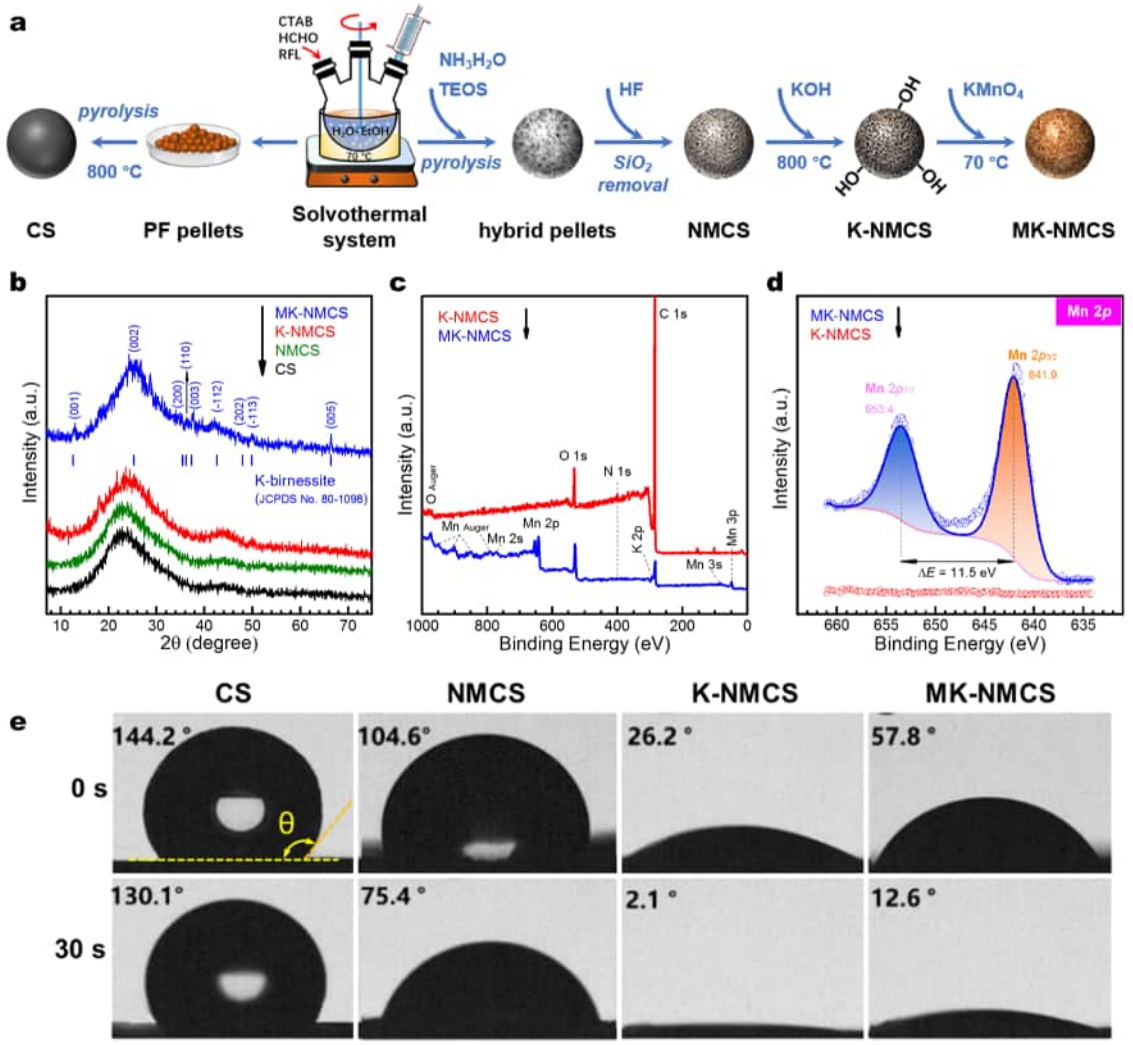

Figure 1. (a) Schematic illustration of the preparation of MnO_2 anchored mesoporous carbon nanocomposites; (b) X-ray diffraction (XRD) patterns; (c) survey X-ray photoelectron spectroscopy (XPS) spectra; (d) Mn 2p XPS region of K-NMCS and MK-NMCS (note: ΔE of the two split components of the Mn 2p peak is about 11.5 eV, indicative of the MnO_2); and (e) water contact angle (θ) evolution of these MnO_2/MCS nanocomposites after contacting with water from the beginning (0 s) to 30 s (30 s).

Tackling heavy metal contamination involves various strategies for wastewater decontamination and water purification.[11] Traditional methods include chemical precipitation, filtration, and ion exchange, but these approaches can be costly and less efficient.[12] Among the cutting-edge technologies, capacitive deionization (CDI) has emerged as a promising method for heavy metal ion removal.[13−16] CDI utilizes an electric field to drive ions from water into porous electrodes, effectively removing contaminants.[17−19] This technology offers several advantages, such as high efficiency, lower energy consumption, and the potential for regeneration of the electrodes, making it a viable solution for mitigating heavy metal pollution and addressing water scarcity challenges.[20−22] So far, a large variety of electrode materials have been extensively used in CDI for capturing heavy metals from water, which can be broadly categorized into nonFaradaic (e.g., carbon-based matter) and Faradaic (charge transfer) materials.[23,24] Among various Faradaic (charge transfer) materials, manganese dioxide (MnO_2) has emerged as a promising electrode material for CDI due to its low cost, high stability, and high theoretical specific capacitance of 1370 F g^{-1}.[25−27] However, like most common transition metal oxides, MnO_2 has a poor electrical conductivity, which limits its CDI performance, such as salt adsorption rate (SAR) and salt adsorption capacity (SAC).[28−30]

To this end, integrating MnO_2 with carbon-based materials of high conductivity appears to be a promising strategy.[31] Since MnO_2 has high pseudocapacitance that contributes to high charge storage capacity and rapid charge/discharge kinetics, carbon-based materials, such as activated carbon or graphene, provide high surface area and electrical conductivity. The combination of MnO_2 and carbon materials can leverage the unique electrochemical properties of both components, yielding manganese dioxide/carbon (MnO_2/C) composite electrodes with superior CDI performance.[32−36] Early studies on MnO_2/C composite electrodes in CDI have demonstrated their effectiveness in both ion removal and heavy metal ion capture. For instance, El-Deen and colleagues reported a graphene-wrapped MnO_2 electrode (MnO_2-nanorods@graphene), which demonstrated distinct SAC (5.01 mg g^{-1}), high salt removal efficiency (~93%), and good recyclability.[32] Chen et al. revealed that composting MnO_2 with multiwalled carbon nanotubes (MWCNTs) can enhance the SAC of the virginal MnO_2 electrode by 4.1 times, and the MnO_2/

https://doi.org/10.1021/acsami.4c18755
ACS Appl. Mater. Interfaces 2025, 17, 13783−13793

MWCNTs composite electrode also showed excellent recyclability and rapid regeneration process.[33] Using an electrodeposition technique, Liu et al. showed that the electrodeposited MnO_2/AC composite electrode presents a superior SAC (9.3 mg g^{-1}) due to the combination of capacitive and Faradaic process.[34] To achieve a better CDI performance of a pristine ordered mesoporous carbon (OMC), Zhao and co-workers decorated OMC with manganese oxide nanoparticles by an impregnation method and showed that the enhanced electrosorption performances were attributed to the Faradaic interfacial process between the guest MnO_2 nanoparticles and the OMC matrix.[35] Besides, it is also shown that graphene-coated single-walled carbon nanotube (SWCNT) aerogels decorated with MnO_2 can be used as freestanding electrodes for superelastic pseudocapacitors, which is also promising for CDI application.[36] Similarly, it has been well-documented in recent reports that integrating MnO_2 with carbon can efficiently improve the CDI performance toward Cu^{2+} and Pb^{2+} ions.[37−40] Birnessite (δ-MnO_2), for example, has been shown as a promising electrode candidate for capacitive capturing Cu^{2+} from water.[37,38] By electrodepositing MnO_2 and polypyrrole (PPy) on the surface of graphene oxide (GO), Zhang et al. prepared a GO/PPy/MnO_2 composite electrode that displays an excellent SAC toward Cu^{2+} ion (38.4 mg g^{-1}).[39] Likewise, Liu and colleagues developed a three-dimensional (3D) graphene/MnO_2 nanocomposite (PGA/MnO_2) electrode that shows high SACs toward various metal ions (e.g., Pb^{2+}, Cu^{2+}, and UO_2^{2+}) due to the 3D porous nanostructure as well as the synergetic action between MnO_2 and graphene.[40] It is well-documented that both nitrogen (N) doping and KOH activation can significantly enhance the specific surface area, wettability, and specific capacitance of carbon-based electrodes, and thereof their CDI performance.[41−43] More recently, it has been shown that N-doping of carbon with nonmetallic elements can greatly improve its affinity toward many metal ions including Pb^{2+} and Cu^{2+} ions.[44,45] However, the interactions between such ions and the MnO_2-decorated carbon doped with nitrogen at CDI platforms have not been explored so far.

Inspired by the aforementioned studies and aimed at elaborating the potentials of MnO_2-decorated N-doped mesoporous carbon electrodes in the capacitive removal of heavy metals, we prepared a set of MnO_2-decorated mesoporous carbon spheres (MnO_2/MCS) and investigated the capacitive removal performance of these MnO_2/MCS electrodes for both Cu^{2+} and Pb^{2+} ions from wastewater at CDI platforms systematically. We elucidated insights into the improvement of the capacitive removal of Cu^{2+} and Pb^{2+} ions over these electrodes via microstructural characterization, electrochemical analysis, and electrochemical desalination experiments. Meanwhile, we evaluated the impacts of cell voltage and salt concentration of the feed solution on the desalination performance, respectively. We also examined the cycling stability of the MnO_2/MCS electrodes and the possible mechanisms of Cu^{2+}/Pb^{2+} uptake. Overall, this work underscores the potential of MnO_2/MCS nanocomposites in addressing both general desalination and specific heavy metal ion removal challenges.

2. MATERIALS AND METHODS

2.1. Chemicals. Cetyltrimethylammonium bromide (CTAB, 99%), potassium permanganate ($KMnO_4$, 99.5%), potassium hydroxide (KOH, 85%), ammonium hydroxide (NH_4OH, 25−28%), resorcinol (RFL, 99%), formaldehyde (HCHO, 37−40%), tetraethyl orthosilicate (TEOS), and hydrofluoric acid (HF, 40%) were purchased from Sinopharm Chemical Co. Sodium chloride (NaCl, 99.5%), copper chloride ($CuCl_2$, 99.99%), and lead chloride ($PbCl_2$, 99.99%) were obtained from Aladdin Chemical Co., Ltd. All chemicals were used as received. Ultrapure deionized water (DI H_2O, 18.2 Ω cm at 25 °C) was used for preparing the solutions.

2.2. Preparation of MnO_2/Mesoporous Carbon Nanocomposites. As depicted in Figure 1a, MnO_2/mesoporous carbon nanocomposites were prepared via a multistep synthesis approach. Typically, 4.0 g of CTAB, 1.1 g of RFL, and 0.2 mL of NH_4OH were first dissolved in a three-neck flask containing an EtOH/water solution (80 mL/200 mL, v/v), to which 1.48 mL of HCHO and 6 mL of TEOS were then added and solvothermally treated at 70 °C for 24 h under moderate stirring conditions (60 rpm). The resulting pellets were collected by centrifugation and rinsed several times with excess DI water and EtOH, followed by drying in an oven at 80 °C overnight. The dry pellets were then pyrolyzed at 800 °C for 2 h under a N_2 atmosphere. After cooling down to room temperature, the synthetic hybrid pellets were further rinsed and etched with 10% HF solution to remove the silicon dioxide (SiO_2) component, yielding N-doped mesoporous carbon spheres denoted as NMCS.

Activation of NMCS pellets by KOH was achieved by mixing 0.5 g of such pellets in 20 mL of KOH solution (100 g L^{-1}) at 80 °C overnight. The obtained dry sample was sequentially pyrolyzed at 800 °C under a N_2 atmosphere, followed by cooling, rinsing with 10% HCl (for removal of residual K^+) and excess water, and drying at 80 °C overnight. The synthetic pellets are denoted by K-NMCS. Further, anchoring manganese oxide onto the above K-NMCS was carried out by hydrothermally mixing 0.2 g of K-NMCS with 50 mL of $KMnO_4$ solution (0.05 M) at 70 °C for 24 h, followed by rinsing with excess water and drying at 80 °C overnight. The MnO_2-loaded sample was denoted by MK-NMCS. For comparison, the pure mesoporous carbon spheres (denoted by CS) were also prepared using the same protocol as that of NMCS without the addition of NH_4OH and TEOS (i.e., the direct pyrolysis route). All synthetic pellets are stored in a glass desiccator before use.

2.3. Materials Characterization and Electrochemical Measurements. X-ray diffraction (XRD), X-ray photoelectron spectroscopy (XPS), scanning electron microscopy (SEM), energy-dispersive X-ray (EDX) spectroscopy, contact angle analysis, and N_2 absorption−desorption measurement were applied to characterize the as-prepared MnO_2/mesoporous carbon nanocomposites. More details about the characterizations are provided in Text S1 (Supporting Information). Electrochemical measurements, including cyclic voltammetry (CV), galvanostatic charge−discharge (GCD), and electrochemical impedance spectroscopy (EIS) were performed in 1.0 M NaCl solution on a CS310H electrochemical workstation (Correst Inc., China). The measurements were conducted with a three-electrode system containing a 1 cm × 2 cm graphite paper precoated with the MnO_2/mesoporous carbon nanocomposites (working electrode), a platinum foil electrode (counter electrode), and an Ag/AgCl (3 M KCl) electrode (reference electrode). A detailed description of the electrochemical measurement is elaborated in Text S2 (Supporting Information).

2.4. Capacitive Deionization Test. The electrodes for CDI performance evaluation were prepared by using the same recipe of electrodes for electrochemical measurements (Text S2). Typically, 50 mg of active materials was mixed and ground with a desired amount of acetylene black and poly(vinylidene fluoride) (PVDF) to achieve a final mass ratio of 8:1:1, followed by dispersing in 4 mL of N, *N*-dimethylformamide (DMF) by sonication for 60 min to form a homogeneous slurry. The slurry was sequentially applied onto a clean graphite paper (5 cm × 5 cm), which was dried in a vacuum at 100 °C overnight before mounting onto the CDI cell (Figure S1).[27] The CDI tests were performed in batch mode under constant voltage conditions. Voltages of 0.6−1.2 V and feed solutions of 100−500 ppm of NaCl solutions were employed to evaluate the influences of cell voltage and feed solution on the CDI performance, respectively. The SAC of the electrode was determined by eq 1

https://doi.org/10.1021/acsami.4c18755
ACS Appl. Mater. Interfaces 2025, 17, 13783−13793

$$\mathrm{SAC} = \frac{(C_0 - C_e)V}{m} \quad (1)$$

where C_0 and C_e represent the initial and the final concentration of the feed solution (mg L^{-1}), respectively, V is the solution volume (mL), and m refers to the total mass of the active electrode material (g). More details on CDI tests are given in Text S3 (Supporting Information).

3. RESULTS AND DISCUSSION

3.1. Physicochemical Characteristics of As-Prepared Materials. The XRD patterns of the as-prepared materials are shown in Figure 1b. All of the patterns are featured by two diffuse humps in 2θ ranges of 10−40 and 40−50° irrespective of the synthetic routes, i.e., direct pyrolysis at 800 °C (CS), doping by nitrogen (NMCS), activating with KOH (K-NMCS), and decorating with MnO_2 (MK-NMCS). These diffuse humps indicate the amorphous nature of these synthetic carbon spheres.[46] It is noteworthy that several tiny peaks arose in the profile of the MnO_2-decorated mesoporous carbon sample upon hydrothermal loading of the Mn species at 70 °C. A comparison with standard PDF cards embedded in MDI Jade (version 6.5) shows that these diffraction peaks are well matched to those of the K-birnessite (JCPDS #80-1098, δ-MnO_2), implying that MnO_2 has been successfully decorated over the mesoporous carbon spheres. XPS analyses of both K-NMCS and MK-NMCS samples further confirm that MnO_2 was completely anchored over the NMCS surface, as evidenced by the Mn 2s, 2p peaks (Figure 1c). Furthermore, the Mn 2p peak was found to show a spin−orbit splitting value of 11.5 eV (Figure 1d), suggesting that Mn exists in an oxidation state of Mn^{4+} in MK-NMCS,[27] in good agreement with the above XRD results.

To examine the surface hydrophilicity of the synthetic samples, we measured the water contact angle (θ) evolution of all of these samples at 0 and 30 s, respectively (Figure 1e). Note that the surface of CS obtained from direct pyrolysis is hydrophobic as indicated by the θ of 144.2 and 130.1° at 0 and 30 s after contact with water. However, after nitrogen doping, the initial θ was 104.6° and then decreased to 75.4° after 30 s. It is well-known that nitrogen doping can create various N-containing functional groups, e.g., amines (−NH_2), imides (−NH−), or pyridinic nitrogen (−C═N−), depending on the doping conditions and the virgin carbon material.[47] Some groups are hydrophilic (such as amines), and others may not be as strongly hydrophilic. A possible explanation for the change in θ of the NMCS is that the hydrophilic sites (i.e., −NH_2) are dominant in the NMCS, which is likely covered by the other hydrophobic groups. The slightly hydrophobic surface of NMCS has been turned into hydrophilic after activation by KOH (θ = 26.2 and 2.1° at 0 and 30 s); this is attributed to the abundant surface hydroxyl groups anchored by alkaline activation.[21] Interestingly, after decorating MnO_2 to the K-NMCS, its hydrophilicity has been decreased a little bit, which is believed to be the replacement of surface hydroxyls (with high hydrophilicity) by [MnO_6] octahedra (with less hydrophilicity than hydroxyls).

The morphological characters of all of these as-prepared samples are depicted in Figure 2. All of the synthetic materials are monodispersed nanospheres with an average particle size of ∼550 nm (Figure 2a−d). The surface morphologies of CS and NMCS are similar (Figure 2a,b), implying that N-doping appears not to have much effect on the surface morphology. However, the following HF-etching process will undoubtedly create massive surface porosity and roughness in the carbon spheres (Figure 2c).[48] Notably, the SEM image of a higher magnification reveals that the surface of K-NMCS is enriched with hierarchical porosity as KOH activation can remove some carbon atoms to introduce abundant defects,[49] thereby significantly increasing its specific surface area.[41] Upon decorating with MnO_2, the resulting MK-NMCS demonstrates a similar surface as K-NMCS, but with less roughness (Figure 2e,f) due to partial filling of the surface pores by MnO_2 particulates. EDX analysis indicates that the elemental compositions of MK-NMCS are C, N, O, K, and Mn (Figure S2), all of which are uniformly dispersed over the surface of K-NMCS materials (Figures 2f and S2). Besides, the atomic percentage of Mn is 9.68% (Figure S2), further confirming the XRD and XPS data. The results of the porosity analysis are illustrated in Figure S3. The Brunauer−Emmett−Teller (BET) surface areas of CS, NMCS, K-NMCS, and MK-NMCS are 299, 686, 1267, and 212 m^2 g^{-1}, respectively (Figure S3a), in good agreement with the SEM images. Note that direct pyrolysis yielded CS with an average pore size of 7.8 nm (Figure S3b), but copolymerization with TEOS coupled with SiO_2 removal can expand the pore size to 11 nm and increase the BET surface area significantly. Interestingly, KOH activation appears to further increase both the BET surface area and the pore, which was also observed elsewhere.[21] Upon decorating with MnO_2, the BET surface area decreased expectedly, but only the mesopores of 15 nm disappeared due to the anchoring of MnO_2 nanoparticles (Figure S3b), indicating that these MnO_2 nanoparticles have a particle size in the range of 5−15 nm, which is favorable for the diffusion and thereof the intercalation of sodium and heavy metal ions due to the much shorter diffusion pathways of nanosized MnO_2 compared to bulk MnO_2.

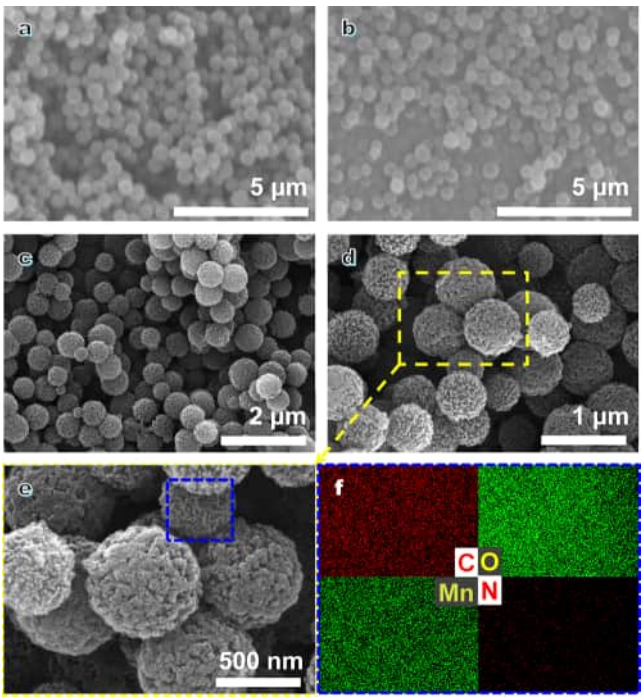

Figure 2. SEM images of as-prepared (a) CS, (b) NMCS, (c) K-NMCS, (d) MK-NMCS, and (e) MK-NMCS of higher magnification and (f) the corresponding energy dispersive X-ray (EDX) elemental mapping (note: the elemental compositions in the blue frame area are shown in Figure S2).

https://doi.org/10.1021/acsami.4c18755
ACS Appl. Mater. Interfaces 2025, 17, 13783−13793

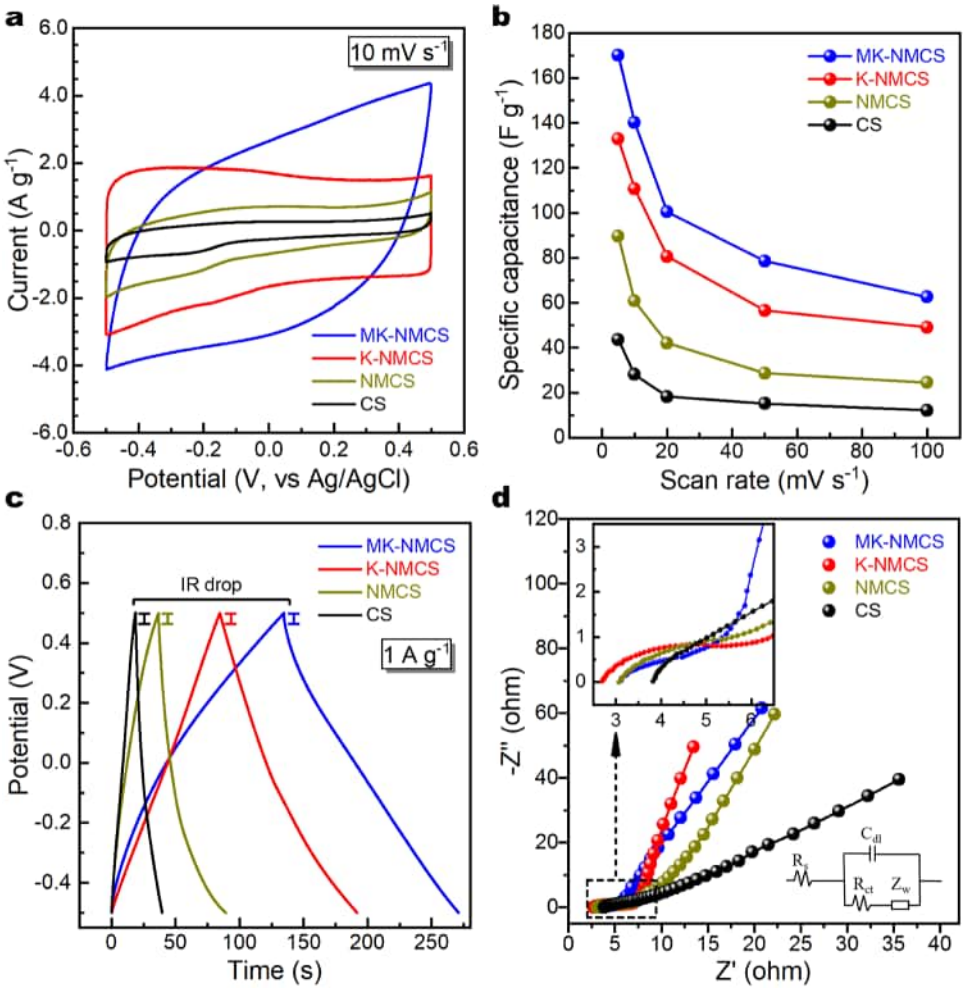

Figure 3. Electrochemical characterizations of all mesoporous carbon nanocomposite electrodes: (a) CV curves at 10 mV s^{-1} in 1.0 M NaCl solution; (b) specific capacitances at different specific currents; (c) GCD curves at 1 A g^{-1} in 1.0 M NaCl solution; (d) Nyquist plots of EIS and the fitting curves, inset in the bottom right corner is the corresponding equivalent circuit.

3.2. Electrochemical Properties of Electrodes. As shown in Figure 3a, the CV profiles of all of these mesoporous carbon composite electrodes expect MK-NMCS obtained in 1.0 M NaCl solution at 10 mV s^{-1} are featured by near-rectangular shapes, indicative of near-ideal capacitive behavior of common carbon-based electrodes.[50] MK-NMCS, in contrast, demonstrated a leaflike-shaped voltammogram, implying a typical less-than-ideal capacitive behavior of redox-active electrodes.[27,51] Specifically, the CV curve is distorted over the potential window of −0.4 to 0.4 V due to the Faradaic reactions ($MnO_2 + Na^+ + e^- \rightleftharpoons MnOONa$) occurring inside the anchored MnO_2.[38,51−54] Moreover, the integrated areas under these CV profiles appear to decrease in the order MK-NMCS > K-NMCS > NMCS > CS, indicating the MK-NMCS electrode shows the largest specific capacitance, and probably the best desalination performance (Table S1). The specific capacitances of these electrodes (calculated using eq S1) are negatively correlated with the specific current as expected (Figure 3b) and decrease clearly in the order MK-NMCS > K-NMCS > NMCS > CS. For instance, the MK-NMCS electrode demonstrated a specific capacitance of 170.1 F g^{-1} at 5 mV s^{-1}, whereas K-NMCS displayed a specific capacitance of 132.9 F g^{-1} (versus those of NMCS and CS electrodes, 89.7 and 43.7 F g^{-1} obtained at 5 mV s^{-1}, respectively). Note that the MK-NMCS electrode with the smallest specific surface area (212 m^2 g^{-1}) shows the highest specific capacitance among all of the electrodes. This is because there is a more important contribution from the Faraday reaction in the MnO_2 particles in addition to the capacitive contribution of the carbon components in the MK-NMCS electrode.[39,55,56]

The GCD curves at 1 A g^{-1} in 1.0 M NaCl solution are of nearly symmetric triangles over one cycle of charge−discharge operation, indicating a well-defined and highly reversible character of the capacitive and/or Faradaic behavior during the GCD operation.[27,34] Note that there are *iR* (current resistance) drops at the beginning of each discharge curve but they are too small to be negotiable (Figure S4). The EIS profiles shown in Figure 3d indicate that the charge-transfer resistances (R_{ct}) of these electrodes are 16.5, 7.3, 3.8, and 4.2 Ω for CS, NMCS, K-NMCS, and MK-NMCS, respectively. This observation confirms that both the nitrogen doping and the KOH activating can greatly reduce the resistance against charge transfer within the carbon materials, thereby boosting the charge migration inside the N-dope carbon electrodes.[21,57] Notably, the R_{ct} of the MK-NMCS electrode is slightly greater than that of the K-NMCS electrode, which is probably due to partial blocking of the mesopores by the anchored MnO_2 with poor electron conductivity. Furthermore, the steep portion in the intermediate and low-frequency regions (also known as the

https://doi.org/10.1021/acsami.4c18755
ACS Appl. Mater. Interfaces 2025, 17, 13783−13793

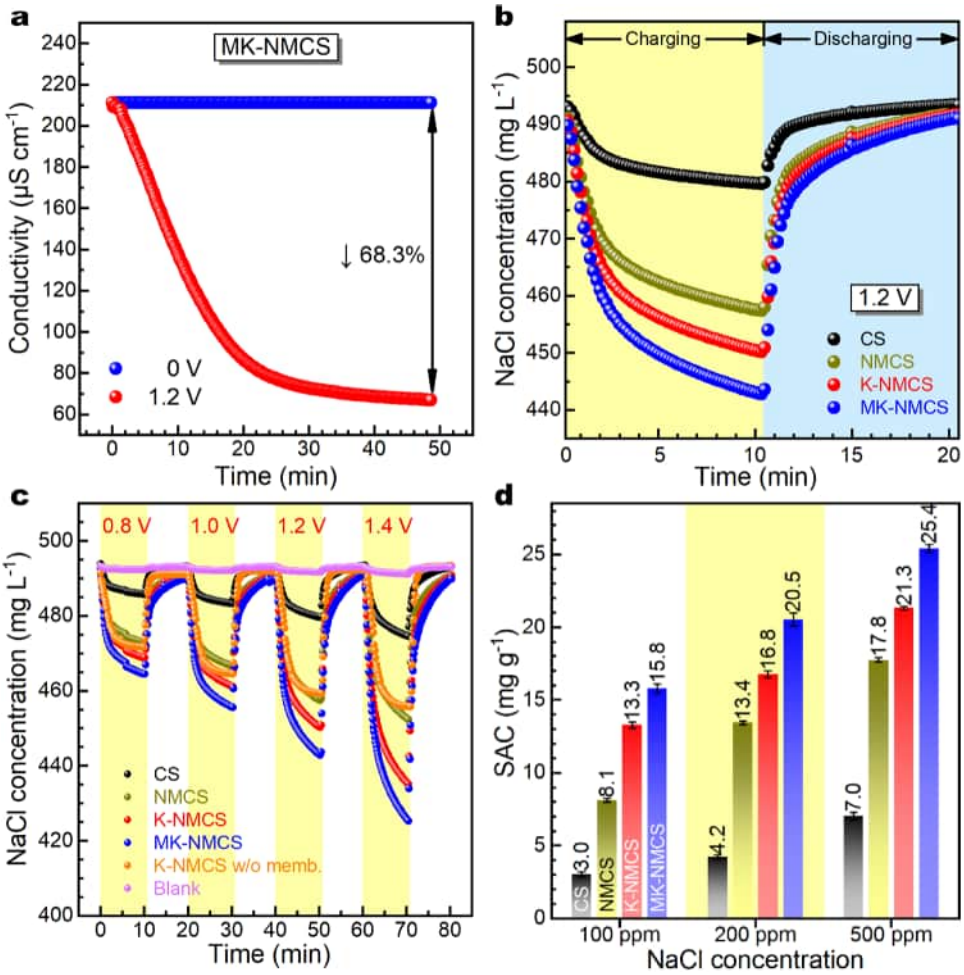

Figure 4. (a) Plot of conductivity versus time in the third CDI operation with MK-NMCS electrodes in 100 mg L^{-1} (1.71 mM) of NaCl solution at 0 and 1.2 V, respectively; (b) plots of NaCl concentration during one cycle of charging−discharging operation in CDI cells with different nanocomposite electrodes in 500 mg L^{-1} of NaCl solution at 1.2 V; (c) plot of NaCl concentration during the charging−discharging operations in 500 mg L^{-1} of NaCl solution at varying voltages (note: "Blank" refers to the graphite paper//graphite paper system, "K-NMCS w/o memb." denotes the K-NMCS//K-NMCS system without (w/o) ion-exchange membranes; both systems are used as reference); (d) comparison of the SACs of mesoporous carbon nanocomposite electrodes applied to feedwaters with varying NaCl concentrations and at a voltage of 1.2 V.

Warburg impedance, Z_w) reflects the frequency-dependent nature of ion transport between the electrolyte and the electrode during the charge−discharge operation. An increase in the slope of the profile indicates a higher level of Warburg impedance. Note that the slopes in the range 10−25 Ω decrease in the order K-NMCS > NMCS > MK-NMCS > CS (Figure 3d), which implies that the CS electrode has the highest interfacial ion migration rate among these electrodes. Interestingly, the MK-NMCS electrode demonstrates a bit higher Z_w as compared to that of the CS. A possible explanation is that the partial blocking of mesopores by MnO_2 hinders the ion migration from the electrolyte to the electrode, as well, thus resulting in a slight increase in the corresponding Warburg impedance.

3.3. Performance of Capacitive Deionization. The CDI performance of these electrodes was evaluated in batch mode on an hybrid capacitive deionization (HCDI) platform with various cathode//anode pairs (Table S1). The pairings were designed based on the unique properties of each electrode (Figure 3) and the importance of prefunctionalization of carbon-based electrodes in HCDI.[58] Initially, we chose the MK-NMCS//K-NMCS pair to study the static adsorption of Na^+ and Cl^- onto the cathodes and the anodes in 100 mg L^{-1} of NaCl solution. It was found that the conductivity remained the same for ∼50 min when no cell potential was applied to the HCDI cell (0 V, Figure 4a), implying no static adsorption took place between the electrodes and the electrolyte. This observation is consistent with other previous reports and is believed to be attributed to the barrier effect of ion-exchange membranes (IEMs).[27,38] When a cell potential of 1.2 V was applied, the conductivity of the feed solution decreased dramatically by 68.3% (equivalent to an SAC of 15.8 mg g^{-1}), indicating the capture of both Na^+ and Cl^- by the electrodes. We further examined the CDI performance of these electrode pairs during one full charge−discharge cycle at 1.2 V in 500 mg L^{-1} of NaCl solution (Figure 4b). Note that the MK-NMCS electrode exhibited greater salt capture than the other electrodes over the same time interval during the charge operation; in other words, the MK-NMCS electrode demonstrated the greatest salt adsorption rate (SAR), followed by K-NMCS, NMCS, and CS. Calculation with eq 1 reveals that the MK-NMCS electrode has the greatest SAC of 25.4 mg g^{-1}, overpassing those of other electrodes (Table S1). This is attributed to the synergistic effect between the cathode and the

https://doi.org/10.1021/acsami.4c18755
ACS Appl. Mater. Interfaces 2025, 17, 13783−13793

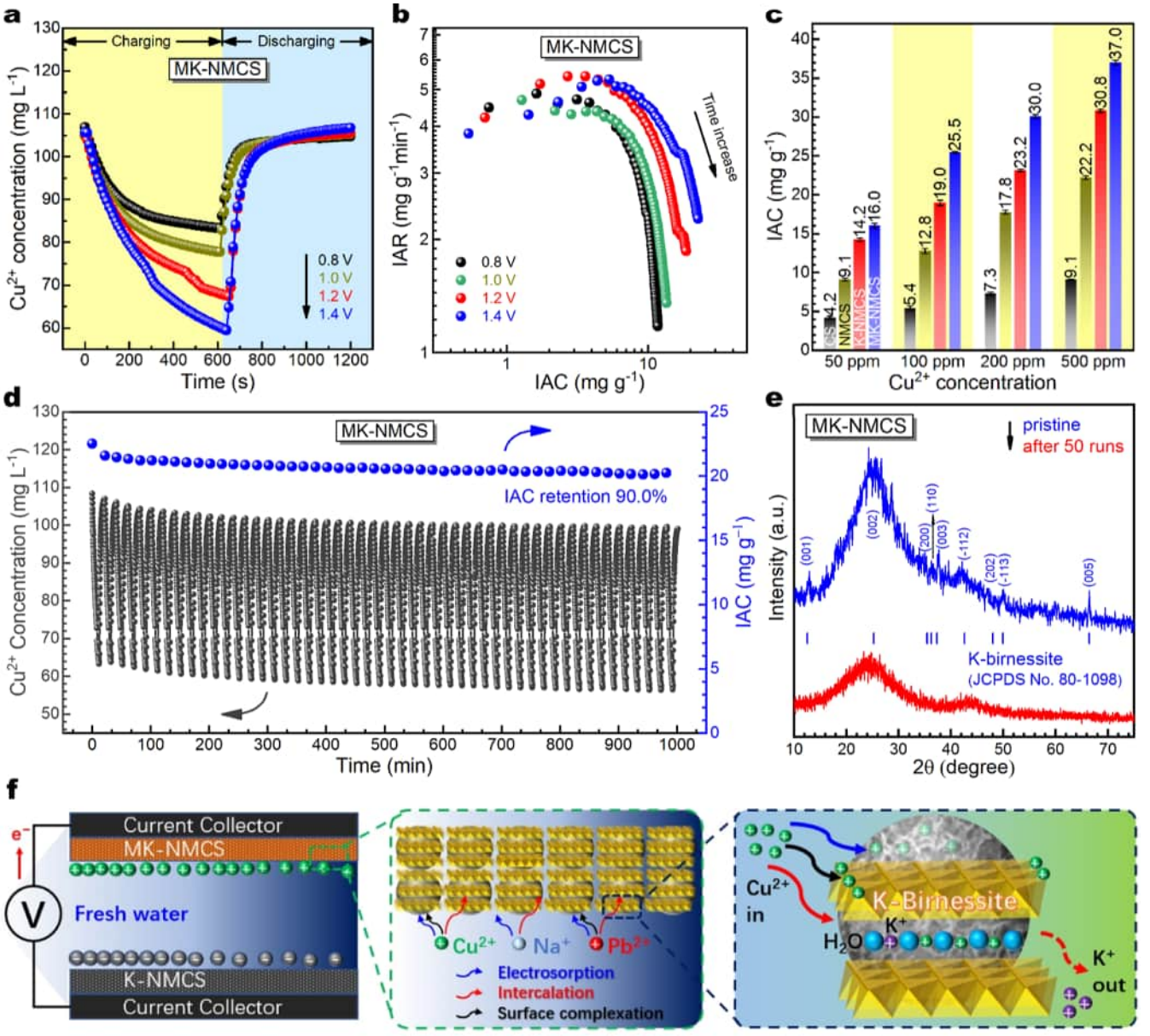

Figure 5. (a) Plots of Cu^{2+} concentration during one cycle of charging−discharging operation in CDI cells with MK-NMCS electrodes in 100 mg L^{-1} of Cu^{2+} solution at varying voltages; (b) Kim-Yoon plots of the MK-NMCS electrodes in 100 mg L^{-1} of Cu^{2+} solution at varying voltages; (c) comparison of IAC of all mesoporous carbon nanocomposite electrodes applied to feedwaters with varying Cu^{2+} concentrations and at a voltage of 1.2 V; (d) cycling stability and the corresponding IAC of the MK-NMCS//K-NMCS electrode system in 100 mg L^{-1} of Cu^{2+} solution at 1.2 V; (e) XRD patterns of the MK-NMCS electrodes before and after 50 runs of CDI operation; (f) proposed mechanism of Cu^{2+} electrosorption and intercalation by MK-NMCS electrodes at CDI platforms.

anode, where the Faradaic reactions within MnO_2 contribute additional Na^+ ion storage beyond simple capacitive behavior, and the electrical and structural properties of carbon improved by N-doping and KOH activation boost its capturing capacity toward Cl^-, allowing for much higher ion capturing capacity.[32,34,56,59,60] Notably, a comparison of these desalination performances indicates that the SAC of the CS//CS pair at 1.2 V was increased by 146.3% after N-doping (Table S1), validating the important contribution of N-doping to the improvement of CDI performance of carbon electrodes.[57,61−63] Likewise, the positive effects of KOH activation and MnO_2 decoration on the desalination performance were demonstrated by the corresponding SAC increments of 23.4 and 24.5%, respectively. During the discharge operation, the regeneration rate of these electrodes also follows the same order MK-NMCS > K-NMCS > NMCS > CS, confirming the excellent reversibility of the electrodes once again (Figure 3c) and implying that applying a reverse voltage is an efficient approach to regenerate the electrodes when there are IEMs within the HCDI cell.

To explore the effects of cell voltage and feed concentration on the SAC of these electrodes, we performed the CDI experiments in 500 mg L^{-1} of NaCl solution at varying cell voltages (0.8−1.4 V) (Figure 4c) and in feed saline with increasing NaCl concentrations (100−500 mg L^{-1}) at 1.2 V (Figure 4d), respectively. It was observed that the NaCl concentration dropped much more rapidly with increasing cell voltage, showing a near-linear increase in SAC for all electrodes

https://doi.org/10.1021/acsami.4c18755
ACS Appl. Mater. Interfaces 2025, 17, 13783−13793

studied (Table S1), which is as expected and consistent with earlier observations.[33,38,45] Note that SACs of the K-NMCS electrode demonstrate a much higher value than those of the K-NMCS electrode without a membrane, verifying the contribution to the SAC from IEMs. For instance, the SAC of the K-NMSC electrode at 1.2 V was increased by 30.8% in the presence of membranes as compared to the counterpart w/o membranes (Table S1). Considering that a cell voltage of 1.4 V usually leads to side reactions such as water splitting (above 1.23 V) and shortening the life span of electrodes,[21,54] like most groups in the CDI community, we chose 1.2 V as the optimal cell voltage. Besides, the salt gradient between the bulk electrolytes and the surface of electrodes is no-double higher in feedwater with higher NaCl concentration, which, in turn, yields a much greater driving force that facilitates the transfer of ions from the bulk electrolytes to the electrodes, thus attaining a higher SAC consequently (Figure 4d). This phenomenon is in good agreement with previous studies.[32,34,57,64] Moreover, the SACs of MK-NMCS electrodes have demonstrated a high SAC comparable to those of other top MnO_2/C-based electrodes reported in the literature so far (Table S2 and Figure S5).

Given the superior performance of the MK-NMCS electrode, synthetic wastewaters containing either Cu^{2+} or Pb^{2+} ions (50−500 mg L^{-1}) were then used to verify its potential for capacitive removal of both HMs at CDI platforms. As shown in Figure 5a, in 100 mg L^{-1} of Cu^{2+} solution, the MK-NMCS electrode also demonstrated the same dependence of ion adsorption capacity (IAC, calculated by eq S2) on cell voltage over the range of 0.8−1.4 V as that in NaCl solution (Figure 4b) during one charge−discharge operation. This trend appears once again in the case of 100 mg L^{-1} of a Pb^{2+} solution (Figure S6a). Further analyses based on the Kim-Yoon plot (Figures 5b and S6b) indicate that applying a higher cell voltage can improve the driving force for ion transfer from the bulk electrolytes to the surface of electrodes, thereby increasing both the IAC and the ion adsorption rate (IAR, calculate by eqs S3 and S4) at a certain time.[13,44] Likewise, the impacts of the Cu^{2+}/Pb^{2+} ion concentration on the IAC were explored over these electrodes at 1.2 V in solutions with varying Cu^{2+}/Pb^{2+} concentrations. Irrespective of the type and concentration of both metals, these electrodes show the same trend based on their IACs toward both ions, decreasing in the order MK-NMCS > K-NMCS > NMCS > CS (Figures 5c and S6c). Note that the IAC of the CS//CS for Cu^{2+} in 100 mg L^{-1} of Cu^{2+} solution was increased by 137% after N-doping (Figure 5c), while a further IAC increment of 48.4% was achieved upon KOH activation (K-NMCS versus NMCS). Similar improvements in ion electrosorption capacity were also observed for the CS, NMCS, and K-NMCS electrode pairs in the case of Pb^{2+} ions (Figure S6c), due to the structural, chemical, and electrical advantages from N-doping and KOH activation (e.g., larger specific surface area, better wettability, better charge transfer ability, and improved specific capacitance).[21,42,45,57] Their IACs also exhibit the same dependence on metal ion concentration in the bulk electrolytes as observed in the case of the NaCl solution. For instance, the IAC of MK-NMCS toward Cu^{2+} is 16.0 mg g^{-1} at 1.2 V in 50 mg L^{-1} of Cu^{2+} solution, whereas it is increased by 59.4, 87.5, and 31.3% in 100, 200, and 500 mg L^{-1} of Cu^{2+} solutions to 25.5, 30.0, and 37.0 mg g^{-1}, respectively (Figure 5c). In addition, the MK-NMCS electrode demonstrates excellent IACs toward both Cu^{2+} and Pb^{2+} ions (e.g., 30.0 and 37.0 mg g^{-1} for Cu^{2+}, 32.2 mg g^{-1} for Pb^{2+} at 1.2 V) under environmentally relevant conditions, which ranks the top of electrodes applied in CDI for capturing both ions,[11,12,15] showcasing its potential for application in heavy metal remediation.

3.4. Recycling Performance and Potential Mechanism. Following the same protocol described elsewhere,[38] we chose K-NMCS and MK-NMCS electrodes to conduct the recycling tests. As illustrated in Figures S7 and S8, the cycling stability of the K-NMCS electrode in 500 mg L^{-1} of NaCl solution at 1.2 V degrades gradually over time regardless of the presence of IEMs, with a slightly faster rate of degeneration in the absence of IEMs (cf. Figures S7 and S8). For instance, the SAC retention of K-NMCS electrodes w/o a membrane is about 95.4% after 15 consecutive cycles of charge and discharge, while it remains up to 100% in the presence of IEMs under the same conditions (yellow-shaded region in Figure S8). This observation further verifies that the IEMs not only improve the salt uptake but also enhance the short-term cycling stability of the electrodes applied in CDI.[21,22,54] As far as long-term cycling stability is concerned, the structural integrity of the electrodes appears to play a more critical role. Although the K-NMCS electrodes show a SAC retention of 100% over the initial 15 cycles in the presence of IEMs, it continues to decline over time to 82.5% after 50 cycles due to the recession of carbon-based electrodes.[27]

In contrast, the MK-NMCS//K-NMCS electrode system shows excellent cycling stability in 500 mg L^{-1} of NaCl solution at 1.2 V, yielding a SAC retention as high as 102.4% after 50 consecutive cycles (Figure S9). Such an abnormal SAC retention (beyond the theoretical value of 100%) is likely to be ascribed to the fact that some of the Na^+ ions are trapped within the MnO_2 lattice during the cycling operations, leading to an apparent SAC that exceeds 100%.[65,66] This is essentially attributed to the intrinsic stability of the electrodes (e.g., the MK-NMCS), the IEMs, and the synergistic effect between the cathode and the anode.[55,67,68] The results of cycling stability tests in 100 ppm of Cu^{2+} and Pb^{2+} solutions are depicted in Figures 5d and S6d, respectively. The MK-NMCS electrodes also exhibit excellent cycling stability and high SAC retentions. After 50 consecutive cycles, the SAC retentions for Cu^{2+} and Pb^{2+} were as high as 90 and 98.5%, respectively. The SAC retention of the MK-NMCS electrode for Cu^{2+} is slightly lower than that for Pb^{2+} ions under the same conditions, even though the hydrated ionic radii of both ions are similar.[69] One possible explanation is that the affinity of MnO_2 for Pb^{2+} ions is stronger than that for Cu^{2+} ions.[40,70] During the charge−discharge process, both ions undergo capacitive adsorption (electrosorption) within carbonaceous components, insertion inside MnO_2 components, and complexation at the external surface of the [MnO_6] octahedral layers. The stronger complexation between Pb^{2+} and the external surface of the [MnO_6] layers may help stabilize the layer configuration. Therefore, the repeated charge−discharge process is likely to impair the structural integrity of the MnO_2 component, which likely induces the collapse (deconstruction) of the MnO_2 crystals in the case of Cu^{2+} with weaker affinity, ultimately leading to a decrease in SAC retention. Our previous report has also shown that gradual phase degradation of Mn oxides occurs over time upon Cu^{2+} ions intercalation/deintercalation.[38] The XRD patterns of the MK-NMCS electrode before and after 50 charge−discharge cycles revealed that the intensity of the MnO_2 diffraction peaks decreased significantly (Figure 5e). This is in good agreement with our earlier

https://doi.org/10.1021/acsami.4c18755
ACS Appl. Mater. Interfaces 2025, 17, 13783−13793

observation,[38] further validating the above speculation of the collapse of MnO_2 crystals after the cycling test.

As mentioned earlier, the N-doped carbon component and the MnO_2 component in the MK-NMCS electrode capture ions by different mechanisms, respectively. Specifically, the N-doped carbon traps Cu^{2+} and Pb^{2+} ions by electrosorption, while MnO_2 achieves ion capturing by a Faraday intercalation reaction ($MnO_2 + 0.5\ M^{2+} + e^- \rightarrow M_{0.5}MnO_2$, $M^{2+} = Cu^{2+}$ or Pb^{2+}). Note that Cu^{2+} is likely to be reduced to elemental copper upon CDI operations due to its higher standard reduction potential (0.1 V versus saturated calomel electrode (SCE)).[37] But our previous study has excluded this electroreduction reaction of Cu^{2+}.[38] Additionally, considering the higher affinity of MnO_2 toward both heavy metals in aqueous solutions, surface complexation reactions between both ions and the external surface of MnO_2 (i.e., $[MnO_6]$ layer) will undoubtedly take place.[65,70] Collectively, the possible capture mechanisms of Cu^{2+} and Pb^{2+} ions at the MK-NMCS electrode are likely regulated by three processes: (i) electrosorption (capacitive behavior) within the N-doped carbon component; (ii) insertion inside the $[MnO_6]$ octahedral interlayers (Faradaic reaction); and (iii) surface complexation at the external surface of the $[MnO_6]$ layers (Figure 5f). Although it has been well demonstrated that both Cu^{2+} and Pb^{2+} ions are inserted into MnO_2 via the Faraday reaction;[38,40] however, due to the degradation of the MnO_2 structure after consecutive cycling in the present study (Figure 5e), it is still challenging to uncover the intercalation and deintercalation of both ions into MnO_2 through microstructural characterization. However, the microscopic evidence in favor of the above ion capture mechanisms can be found in MnO_2/C,[37,38] $W_{18}O_{19}$/C[16], and MoO_2/C electrodes.[45]

4. CONCLUSIONS

A group of MnO_2-decorated mesoporous carbon nanocomposites was prepared via a multistep approach and then evaluated as electrodes for capturing Na^+, Cu^{2+}, and Pb^{2+} ions from wastewaters on an HCDI platform. Benefiting from the intrinsic property of the electrodes, the IEMs, and the synergistic effect between the cathode and the anode, the electrode pair of MK-NMCS//K-NMCS demonstrates the best desalination performance among the electrodes studied, yielding SAC maximums of 33.2 mg g^{-1} (1.4 V) and 25.4 mg g^{-1} (1.2 V) in 500 mg L^{-1} of NaCl solution, respectively. Additionally, the MK-NMCS electrode also shows superior capacities toward Cu^{2+} and Pb^{2+} ions, offering an IAC as high as 30.0 and 32.2 mg g^{-1} in 200 mg L^{-1} of Cu^{2+} or Pb^{2+}-containing note solutions at 1.2 V, respectively. The cycling results reveal that the presence of IEMs can improve the short-term cycling stability and that the MK-NMCS electrode demonstrates excellent cycling stability for all metal ions, attaining SAC retentions of 102.4, 90, and 98.5% over 50 consecutive charge−discharge cycles for Na^+, Cu^{2+}, and Pb^{2+} ions, respectively. Mechanism analysis suggests that capacitive electrosorption (by the mesoporous carbon sphere), intercalation (within the MnO_2), and surface complexation (over the MnO_2 layer, particularly in the case of Cu^{2+} ions) are probably responsible for the sequestration of Cu^{2+} and Pb^{2+} ions. Overall, our findings underscore the potential of the HCDI platform with the MnO_2-decorated mesoporous carbon sphere, particularly the MK-NMCS//K-NMCS electrodes as an efficient toolbox for the remediation of wastewater contaminated by either Cu^{2+} and Pb^{2+} ions. Future studies on the preference of MK-NMCS//K-NMCS electrodes toward specific ions are necessary for fully exploring their potential for ion separation and the recovery of crucial elements from waste streams.

ASSOCIATED CONTENT

Supporting Information

The Supporting Information is available free of charge at https://pubs.acs.org/doi/10.1021/acsami.4c18755.

Supporting texts (S1−S3), tables (S1 and S2), and figures (S1−S9): CDI setup, N_2 absorption−desorption isotherms, pore size distributions, EDX spectrum, electrochemical characterizations, and CDI deionization performance (PDF)

AUTHOR INFORMATION

Corresponding Author

Feihu Li − *Collaborative Innovation Center of Atmospheric Environment and Equipment Technology, Jiangsu Key Laboratory of Atmospheric Environment Monitoring and Pollution Control, School of Environmental Science and Engineering, Nanjing University of Information Science and Technology, Nanjing 210044, China; NUIST Reading Academy, Nanjing University of Information Science and Technology, Nanjing 210044, China;* orcid.org/0000-0002-2969-8276; Email: fhli@nuist.edu.cn

Authors

Jie Jin − *Collaborative Innovation Center of Atmospheric Environment and Equipment Technology, Jiangsu Key Laboratory of Atmospheric Environment Monitoring and Pollution Control, School of Environmental Science and Engineering, Nanjing University of Information Science and Technology, Nanjing 210044, China*

Yang Bao − *Collaborative Innovation Center of Atmospheric Environment and Equipment Technology, Jiangsu Key Laboratory of Atmospheric Environment Monitoring and Pollution Control, School of Environmental Science and Engineering, Nanjing University of Information Science and Technology, Nanjing 210044, China;* orcid.org/0000-0002-5588-2042

Complete contact information is available at: https://pubs.acs.org/10.1021/acsami.4c18755

Notes

The authors declare no competing financial interest.

An earlier version of this manuscript has been deposited on the preprint server ChemRxiv (https://doi.org/10.26434/chemrxiv-2024-7j7cn).

ACKNOWLEDGMENTS

The work was financially supported by the Innovation Program for Postgraduate Research of Jiangsu Province (SJKY19-0977), the Top-notch Academic Programs Project, and the Priority Academic Program Development (PAPD) of Jiangsu Higher Education Institutions.

REFERENCES

(1) Yu, C. China's Water Crisis Needs More Than Words. *Nature* **2011**, *470* (7334), 307.

(2) Eliasson, J. The Rising Pressure of Global Water Shortages. *Nature* **2015**, *517* (7532), 6.

(3) Zhang, Y.; Zheng, H.; Zhang, X.; Leung, L. R.; Liu, C.; Zheng, C.; Guo, Y.; Chiew, F. H. S.; Post, D.; Kong, D.; Beck, H. E.; Li, C.; Blöschl, G. Future Global Streamflow Declines Are Probably More Severe Than Previously Estimated. *Nat. Water* **2023**, *1* (3), 261−271.
(4) Stocker, T. F.; Raible, C. C. Climate Change - Water Cycle Shifts Gear. *Nature* **2005**, *434* (7035), 830−833.
(5) Kümmerer, K.; Dionysiou, D. D.; Olsson, O.; Fatta-Kassinos, D. A Path to Clean Water. *Science* **2018**, *361* (6399), 222−224.
(6) Vega, F. A.; Weng, L. P. Speciation of Heavy Metals in River Rhine. *Water Res.* **2013**, *47* (1), 363−372.
(7) He, M. C.; Wang, Z. J.; Tang, H. X. The Chemical, Toxicological and Ecological Studies in Assessing the Heavy Metal Pollution in Le An River, China. *Water Res.* **1998**, *32* (2), 510−518.
(8) Cukrov, N.; Cmuk, P.; Mlakar, M.; Omanovic, D. Spatial Distribution of Trace Metals in the Krka River, Croatia: An Example of the Self-Purification. *Chemosphere* **2008**, *72* (10), 1559−1566.
(9) Mitra, S.; Chakraborty, A. J.; Tareq, A.; Bin Emran, T.; Nainu, F.; Khusro, A.; Idris, A. M.; Khandaker, M. U.; Osman, H.; Alhumaydhi, F. A.; Simal-Gandara, J. Impact of Heavy Metals on the Environment and Human Health: Novel Therapeutic Insights to Counter the Toxicity. *J. King Saud Univ. Sci.* **2022**, *34* (3), No. 101865.
(10) Yu, Y. L.; Yang, W. Y.; Hara, A.; Asayama, K.; Roels, H. A.; Nawrot, T. S.; Staessen, J. A. Public and Occupational Health Risks Related to Lead Exposure Updated According to Present-Day Blood Lead Levels. *Hypertens. Res.* **2023**, *46* (2), 395−407.
(11) Fu, F. L.; Wang, Q. Removal of Heavy Metal Ions from Wastewaters: A Review. *J. Environ. Manage.* **2011**, *92* (3), 407−418.
(12) Al-Saydeh, S. A.; El-Naas, M. H.; Zaidi, S. J. Copper Removal from Industrial Wastewater: A Comprehensive Review. *J. Ind. Eng. Chem.* **2017**, *56*, 35−44.
(13) Huang, Z.; Lu, L.; Cai, Z. X.; Ren, Z. J. Individual and Competitive Removal of Heavy Metals Using Capacitive Deionization. *J. Hazard. Mater.* **2016**, *302*, 323−331.
(14) Su, X.; Kushima, A.; Halliday, C.; Zhou, J.; Li, J.; Hatton, T. A. Electrochemically-mediated Selective Capture of Heavy Metal Chromium and Arsenic Oxyanions from Water. *Nat. Commun.* **2018**, *9*, No. 4701.
(15) Chen, R.; Sheehan, T.; Ng, J. L.; Brucks, M.; Su, X. Capacitive Deionization and Electrosorption for Heavy Metal Removal. *Environ. Sci.: Water Res. Technol.* **2020**, *6* (2), 258−282.
(16) Mao, M. L.; Yan, T. T.; Shen, J. J.; Zhang, J. P.; Zhang, D. S. Capacitive Removal of Heavy Metal Ions from Wastewater via an Electro-adsorption and Electro-reaction Coupling Process. *Environ. Sci. Technol.* **2021**, *55* (5), 3333−3340.
(17) Wang, J. C.; Yuan, J. H.; Gao, H. W.; Yu, F.; Ma, J. Recent Advances on Capacitive Deionization for Defluorination: From Electrode Materials to Engineering Application. *Chem. Eng. J.* **2024**, *480*, No. 147986.
(18) Gao, M.; Chen, W. Q. Engineering Strategies toward Electrodes Stabilization in Capacitive Deionization. *Coord. Chem. Rev.* **2024**, *505*, No. 215695.
(19) Zhou, X. L.; Shu, S. R.; Ye, X. Y.; Li, Z. J. Engineering Faradaic Electrode Materials for High-efficiency Water Desalination. *Small* **2024**, *20* (32), No. 2400047.
(20) Anderson, M. A.; Cudero, A. L.; Palma, J. Capacitive Deionization as an Electrochemical Means of Saving Energy and Delivering Clean Water. Comparison to Present Desalination Practices: Will It Compete? *Electrochim. Acta* **2010**, *55* (12), 3845−3856.
(21) Porada, S.; Zhao, R.; van der Wal, A.; Presser, V.; Biesheuvel, P. M. Review on the Science and Technology of Water Desalination by Capacitive Deionization. *Prog. Mater. Sci.* **2013**, *58* (8), 1388−1442.
(22) Suss, M. E.; Porada, S.; Sun, X.; Biesheuvel, P. M.; Yoon, J.; Presser, V. Water Desalination via Capacitive Deionization: What Is It and What Can We Expect from It? *Energy Environ. Sci.* **2015**, *8* (8), 2296−2319.
(23) Srimuk, P.; Su, X.; Yoon, J.; Aurbach, D.; Presser, V. Charge-transfer Materials for Electrochemical Water Desalination, Ion Separation and the Recovery of Elements. *Nat. Rev. Mater.* **2020**, *5* (7), 517−538.
(24) Xu, Z. H.; Pang, Z. B.; Yan, X. F.; Ebaid, M. S.; Jiang, X. H.; Thabet, H. K.; Xu, X. T.; Jiang, D.; Yu, L. M. Transition Metal Oxide Electrode Materials for Capacitive Deionization. *Chem. Eng. J.* **2024**, *501*, No. 157257.
(25) Sassin, M. B.; Chervin, C. N.; Rolison, D. R.; Long, J. W. Redox Deposition of Nanoscale Metal Oxides on Carbon for Next-Generation Electrochemical Capacitors. *Acc. Chem. Res.* **2013**, *46* (5), 1062−1074.
(26) Byles, B. W.; Cullen, D. A.; More, K. L.; Pomerantseva, E. Tunnel Structured Manganese Oxide Nanowires as Redox Active Electrodes for Hybrid Capacitive Deionization. *Nano Energy* **2018**, *44*, 476−488.
(27) Jin, J.; Li, M.; Tang, M. T.; Li, Y.; Liu, Y. Y.; Cao, H.; Li, F. H. Phase- and Crystallinity-Tailorable MnO_2 as an Electrode for Highly Efficient Hybrid Capacitive Deionization (HCDI). *ACS Sustainable Chem. Eng.* **2020**, *8* (30), 11424−11434.
(28) Chen, Y.; Pu, S. Y.; Zhang, Z.; Gao, M.; Deng, W. Y.; Ao, T. Q.; Chen, W. Q. The Morphologic Dependence of MnO_2 Electrodes in Capacitive Deionization Process. *Chem. Eng. J.* **2024**, *498*, No. 155276.
(29) Nie, L. J.; Wang, L.; Wang, X. D.; He, M. L.; Wang, J.; Lv, Y. T.; Miao, R.; An, J. J.; Hao, J. J.; Wang, J. Q.; Ren, Y. N. Enhancing Copper Recycling through Synergistic Valence Conversions in MnOx-modified Capacitive Deionization Electrodes. *Chem. Eng. J.* **2024**, *485*, No. 149960.
(30) Li, Y. L.; Wang, Y.; Cai, Y. M.; Fang, R. L.; Zhang, L. The Exploration and Comparison of Adsorption Mechanisms in MnO_2 with Different Crystal Structures for Capacitive Deionization. *Desalination* **2024**, *577*, No. 117387.
(31) Zhao, Y. S.; Zhang, L.; Huang, S. J.; Fang, R. L.; Zhang, S. S.; Wang, Y. Oxygen Vacancy Enhancing Intrinsic Conductivity of rGO@MnO_{2-x} Electrode for Efficient Hybrid Capacitive Deionization. *J. Environ. Chem. Eng.* **2024**, *12* (1), No. 111883.
(32) El-Deen, A. G.; Barakat, N. A. M.; Kim, H. Y. Graphene Wrapped MnO_2-nanostructures as Effective and Stable Electrode Materials for Capacitive Deionization Desalination Technology. *Desalination* **2014**, *344*, 289−298.
(33) Chen, B. W.; Wang, Y. F.; Chang, Z.; Wang, X. W.; Li, M. X.; Liu, X.; Zhang, L. X.; Wu, Y. P. Enhanced Capacitive Desalination of MnO_2 by Forming Composite with Multi-walled Carbon Nanotubes. *RSC Adv.* **2016**, *6* (8), 6730−6736.
(34) Liu, Y. H.; Hsi, H. C.; Li, K. C.; Hou, C. H. Electrodeposited Manganese Dioxide/Activated Carbon Composite As a High-Performance Electrode Material for Capacitive Deionization. *ACS Sustainable Chem. Eng.* **2016**, *4* (9), 4762−4770.
(35) Zhao, C. X.; Lv, X. Y.; Li, J. S.; Xie, T.; Qi, Y. Y.; Chen, W. Manganese Oxide Nanoparticles Decorated Ordered Mesoporous Carbon Electrode for Capacitive Deionization of Brackish Water. *J. Electrochem. Soc.* **2017**, *164* (13), E505−E511.
(36) Zhao, Y. P.; Li, M. P.; Liu, S. Y.; Islam, M. F. Superelastic Pseudocapacitors from Freestanding MnO_2-Decorated Graphene-Coated Carbon Nanotube Aerogels. *ACS Appl. Mater. Interfaces* **2017**, *9* (28), 23810−23819.
(37) Yang, X.; Liu, L. H.; Tan, W. F.; Qiu, G. H.; Liu, F. High-performance Cu^{2+} Adsorption of Birnessite Using Electrochemically Controlled Redox Reactions. *J. Hazard. Mater.* **2018**, *354*, 107−115.
(38) Bao, Y.; Jin, J.; Ma, M. Y.; Li, M.; Li, F. H. Ion Exchange Conversion of Na-Birnessite to Mg-Buserite for Enhanced and Preferential Cu2+ Removal via Hybrid Capacitive Deionization. *ACS Appl. Mater. Interfaces* **2022**, *14* (41), 46646−46656.
(39) Zhang, Y. J.; Wang, Y. A.; Xue, J. Q.; Tang, C. B. MnO_2-Coated Graphene/Polypyrrole Hybrids for Enhanced Capacitive Deionization Performance of Cu2+ Removal. *Ind. Eng. Chem. Res.* **2022**, *61* (10), 3582−3590.
(40) Zhou, J. P.; Pei, Z. Y.; Li, N.; Han, S. T.; Li, Y. P.; Chen, Q.; Sui, Z. Y. Synthesis of 3D Graphene/MnO_2 Nanocomposites with

https://doi.org/10.1021/acsami.4c18755
ACS Appl. Mater. Interfaces 2025, 17, 13783−13793

Hierarchically Porous Structure for Water Purification. *J. Porous Mater.* **2022**, *29* (4), 983−990.
(41) He, R.; Neupane, M.; Zia, A.; Huang, X. Z.; Bowers, C.; Wang, M.; Lu, J.; Yang, Y. C.; Dong, P. Binder-free Wood Converted Carbon for Enhanced Water Desalination Performance. *Adv. Funct. Mater.* **2022**, *32* (49), No. 2208040.
(42) Paraknowitsch, J. P.; Thomas, A. Doping Carbons beyond Nitrogen: an Overview of Advanced Heteroatom Doped Carbons with Boron, Sulphur and Phosphorus for Energy Applications. *Energy Environ. Sci.* **2013**, *6* (10), 2839−2855.
(43) Liu, P. Y.; Yan, T. T.; Shi, L. Y.; Park, H. S.; Chen, X. C.; Zhao, Z. G.; Zhang, D. S. Graphene-based Materials for Capacitive Deionization. *J. Mater. Chem. A* **2017**, *5* (27), 13907−13943.
(44) Wang, Z. R.; Huang, X. H.; Tong, Y. Z. D.; Qin, D. Y.; Wang, T.; Liu, Q.; Hu, G. Z. N, P-doping Tuning the Coordination Structure of Carbon Electrode for Efficiency of Copper Ions Capacitance Deionization. *Desalination* **2024**, *571*, No. 117062.
(45) Luo, J. Y.; Mu, J. C.; Li, X. Y.; Liu, B. J. High Capacitive Removal of Pb^{2+} from Wastewater and Mechanism Study over MoO_2@N-Doped Hollow Carbon Sphere Anodes. *Acs ES&T Water* **2023**, *3* (2), 429−437.
(46) Zhang, S.; Li, F. H.*Integrating of Nickel Hexacyanoferrate with Hollow Mesoporous Carbon Spheres (HMCSs) for Highly Efficient Capacitive Deionization*; ChemRxiv, 2024. DOI: 10.26434/chemrxiv-2024-3kk6v.
(47) Wang, P. S.; Ma, W. T.; Xue, S.; Wang, L.; Chen, Y.; Wang, Y. L. N-doped Carbon Nanosheets Assembled Microspheres for More Effective Capacitive Deionization. *Sep. Purif. Technol.* **2021**, *276*, No. 119336.
(48) Wang, H. J.; Jiang, S. J.; Yu, H. J.; Deng, K.; Wang, Z. Q.; Li, X. N.; Xu, Y.; Wang, L. Interface Engineering of Superhydrophobic Octadecanethiol-functionalized Hollow Mesoporous Carbon Spheres for Alkaline Oxygen Reduction to Hydrogen Peroxide. *J. Mater. Chem. A* **2023**, *11* (25), 13633−13639.
(49) Tian, K. S.; Wang, J. Y.; Cao, L.; Yang, W.; Guo, W. C.; Liu, S. H.; Li, W.; Wang, F. Y.; Li, X. A.; Xu, Z. P.; Wang, Z. B.; Wang, H. Y.; Hou, Y. L. Single-site Pyrrolic-Nitrogen-doped sp(2)-hybridized Carbon Materials and Their Pseudocapacitance. *Nat. Commun.* **2020**, *11*, No. 3884.
(50) Deng, L. J.; Zhu, G.; Wang, J. F.; Kang, L. P.; Liu, Z. H.; Yang, Z. P.; Wang, Z. L. Graphene-MnO_2 and Graphene Asymmetrical Electrochemical Capacitor with a High Energy Density in Aqueous Electrolyte. *J. Power Sources* **2011**, *196* (24), 10782−10787.
(51) Leong, Z. Y.; Yang, H. Y. A Study of MnO_2 with Different Crystalline Forms for Pseudocapacitive Desalination. *ACS Appl. Mater. Interfaces* **2019**, *11* (14), 13176−13184.
(52) Wei, W. F.; Cui, X. W.; Chen, W. X.; Ivey, D. G. Manganese Oxide-based Materials as Electrochemical Supercapacitor Electrodes. *Chem. Soc. Rev.* **2011**, *40* (3), 1697−1721.
(53) Yang, J.; Zou, L. D.; Song, H. H. Preparing MnO_2/PSS/CNTs Composite Electrodes by Layer-by-Layer Deposition of MnO_2 in the Membrane Capacitive Deionisation. *Desalination* **2012**, *286*, 108−114.
(54) Zhang, C. Y.; He, D.; Ma, J. X.; Tang, W. W.; Waite, T. D. Faradaic Reactions in Capacitive Deionization (CDI) - Problems and Possibilities: A Review. *Water Res.* **2018**, *128*, 314−330.
(55) Li, P. X.; Yang, Y. B.; Shi, E. Z.; Shen, Q. C.; Shang, Y. Y.; Wu, S. T.; Wei, J. Q.; Wang, K. L.; Zhu, H. W.; Yuan, Q.; Cao, A. Y.; Wu, D. H. Core-Double-Shell, Carbon Nanotube@Polypyrrole@MnO_2 Sponge as Freestanding, Compressible Supercapacitor Electrode. *ACS Appl. Mater. Interfaces* **2014**, *6* (7), 5228−5234.
(56) Tan, G. C.; Wan, S.; Mei, S. C.; Gong, B.; Qian, C.; Chen, J. J. Boosted Brackish Water Desalination and Water Softening by Facilely Designed MnO_2/Hierarchical Porous Carbon as Capacitive Deionization Electrode. *Water Res. X* **2023**, *19*, No. 100182.
(57) Liu, Y.; Chen, T. Q.; Lu, T.; Sun, Z.; Chua, D. H. C.; Pan, L. K. Nitrogen-doped Porous Carbon Spheres for Highly Efficient Capacitive Deionization. *Electrochim. Acta* **2015**, *158*, 403−409.
(58) Wu, T. T.; Wang, G.; Wang, S. Y.; Zhan, F.; Fu, Y.; Qiao, H. Y.; Qiu, J. S. Highly Stable Hybrid Capacitive Deionization with a MnO_2 Anode and a Positively Charged Cathode. *Environ. Sci. Technol. Lett.* **2018**, *5* (2), 98−102.
(59) Yang, J.; Zou, L. D.; Song, H. H.; Hao, Z. P. Development of Novel MnO_2/Nanoporous Carbon Composite Electrodes in Capacitive Deionization Technology. *Desalination* **2011**, *276* (1−3), 199−206.
(60) Zhang, B. S.; Li, J. J.; Hu, B.; Wang, Y. W.; Shang, X. H.; Nie, P. F.; Yang, J. M.; Liu, J. Y. Flexible δ-MnO_2 Nanosheet-infixed Porous Carbon Nanofibers for Capacitive Deionization. *Electrochim. Acta* **2023**, *443*, No. 141929.
(61) Wang, Z.; Yan, T. T.; Fang, J. H.; Shi, L. Y.; Zhang, D. S. Nitrogen-doped Porous Carbon Derived from a Bimetallic Metal-Organic Framework as Highly Efficient Electrodes for Flow-through Deionization Capacitors. *J. Mater. Chem. A* **2016**, *4* (28), 10858−10868.
(62) Li, Y.; Qi, J. W.; Li, J. S.; Shen, J. M.; Liu, Y. X.; Sun, X. Y.; Shen, J. Y.; Han, W. Q.; Wang, L. J. Nitrogen-Doped Hollow Mesoporous Carbon Spheres for Efficient Water Desalination by Capacitive Deionization. *ACS Sustainable Chem. Eng.* **2017**, *5* (8), 6635−6644.
(63) Zhang, L. Y.; Wang, R.; Chai, W. C.; Ma, M. Y.; Li, L. K. Controllable Preparation of a N-Doped Hierarchical Porous Carbon Framework Derived from ZIF-8 for Highly Efficient Capacitive Deionization. *ACS Appl. Mater. Interfaces* **2023**, *15* (41), 48800−48809.
(64) Bao, Y.; Hao, J. X.; Zhang, S.; Zhu, D. C.; Li, F. H. Structural/Compositional-Tailoring of Nickel Hexacyanoferrate Electrodes for Highly Efficient Capacitive Deionization. *Small* **2023**, *19* (34), No. 2300384.
(65) Jin, J.; Li, M.; Tang, M.; Li, Y.; Liu, Y.; Cao, H.; Li, F.*Tailorable Phase and Structural MnO_2 as Electrode for Highly Efficient Hybrid Capacitive Desalination (HCDI)*; ChemRxiv, 2019. DOI: 10.26434/chemrxiv.10291976.v1.
(66) Lyu, L.; Seong, K. D.; Kim, J. M.; Zhang, W.; Jin, X. Z.; Kim, D. K.; Jeon, Y.; Kang, J.; Piao, Y. Z. CNT/High Mass Loading MnO_2/Graphene-grafted Carbon Cloth Electrodes for High-energy Asymmetric Supercapacitors. *Nano-Micro Lett.* **2019**, *11* (1), No. 88.
(67) Du, L. H.; Yang, P. H.; Yu, X.; Liu, P. Y.; Song, J. H.; Mai, W. J. Flexible Supercapacitors Based on Carbon Nanotube/MnO_2 Nanotube Hybrid Porous Films for Wearable Electronic Devices. *J. Mater. Chem. A* **2014**, *2* (41), 17561−17567.
(68) Ramezani, M.; Fathi, M.; Mahboubi, F. Facile Synthesis of Ternary MnO_2/Graphene Nanosheets/Carbon Nanotubes Composites with High Rate Capability for Supercapacitor Applications. *Electrochim. Acta* **2015**, *174*, 345−355.
(69) Nightingale, E. R. Phenomenological Theory of Ion Solvation - Effective Radii of Hydrated Ions. *J. Phys. Chem. A* **1959**, *63* (9), 1381−1387.
(70) Li, Y.; Zhao, X. P.; Wu, J. T.; Gu, X. Y. Surface Complexation Modeling of Divalent Metal Cation Adsorption on Birnessite. *Chem. Geol.* **2020**, *551*, No. 119774.